



The internal dynamics of the Local Group dwarf elliptical galaxies NGC 147, 185 and 205

Sven de Rijcke, Philippe Prugniel, F. Simien, Herwig Dejonghe

► To cite this version:

Sven de Rijcke, Philippe Prugniel, F. Simien, Herwig Dejonghe. The internal dynamics of the Local Group dwarf elliptical galaxies NGC 147, 185 and 205. *Monthly Notices of the Royal Astronomical Society*, 2006, 369, pp.1321-1333. 10.1111/j.1365-2966.2006.10377.x . hal-03796925

HAL Id: hal-03796925

<https://hal.science/hal-03796925>

Submitted on 5 Oct 2022

HAL is a multi-disciplinary open access archive for the deposit and dissemination of scientific research documents, whether they are published or not. The documents may come from teaching and research institutions in France or abroad, or from public or private research centers.

L'archive ouverte pluridisciplinaire **HAL**, est destinée au dépôt et à la diffusion de documents scientifiques de niveau recherche, publiés ou non, émanant des établissements d'enseignement et de recherche français ou étrangers, des laboratoires publics ou privés.

The internal dynamics of the Local Group dwarf elliptical galaxies NGC 147, 185 and 205[★]

S. De Rijcke,^{1†‡} P. Prugniel,^{2,3} F. Simien² and H. Dejonghe¹

¹*Sterrenkundig Observatorium, Universiteit Gent, Krijgslaan 281, S9, B-9000, Gent, Belgium*

²*CRAL-Observatoire de Lyon, 9 Av. C. André, 69561 Saint-Genis Laval, France*

³*GEPI Observatoire de Paris, 5, place Jules Janssen, 92195 Meudon Cedex, France*

Accepted 2006 March 23. Received 2006 February 10; in original form 2005 October 25

ABSTRACT

We present three-integral dynamical models for the three Local Group dwarf elliptical galaxies: NGC 147, 185 and 205. These models are fitted to the Two-Micron All-Sky Survey (2MASS) *J*-band surface-brightness distribution and the major-axis kinematics (mean streaming velocity and velocity dispersion) and, in the case of NGC 205, also to the minor-axis kinematics. The kinematical information extends out to $2R_e$ in the case of NGC 205 and out to about $1R_e$ in the case of NGC 147 and 185. It is the first time models are constructed for the Local Group dwarf ellipticals (dEs) that allow for the presence of dark matter at large radii and that are constrained by kinematics out to at least one half-light radius. The *B*-band mass-to-light ratios of all the three galaxies are rather similar, $(M/L)_B \approx 3\text{--}4 M_\odot/L_{\odot,B}$. Within the inner two half-light radii, about 40–50 per cent of the mass is in the form of dark matter, so dEs contain about as much dark matter as bright ellipticals.

Based on their appreciable apparent flattening, we modelled NGC 205 and 147 as being viewed edge-on. For NGC 185, having a much rounder appearance on the sky, we produced models for different inclinations. NGC 205 and 147 have a relatively isotropic velocity dispersion tensor within the region where the internal dynamics are strongly constrained by the data. Our estimated inclination for NGC 185 is $i \approx 50^\circ$ because in that case the model has an intrinsic flattening close to the peak of the intrinsic shape distribution of dEs and it, like the best-fitting models for NGC 147 and 205, is nearly isotropic. We also show that the dynamical properties of the bright nucleus of NGC 205 are not unlike those of a massive globular cluster.

Key words: galaxies: dwarf – galaxies: individual: NGC 147 – galaxies: individual: NGC 185 – galaxies: individual: NGC 205.

1 INTRODUCTION

From the days of the great comet-hunter, Charles Messier, up to well into the 20th century, NGC 205 has been the only known member of the class of objects that we now call dwarf ellipticals (dEs) (Messier 1798). dEs are faint ($M_B \geq -18$ mag) galaxies with diffuse, approximately exponentially declining surface-brightness profiles and smooth elliptical isophotes (Ferguson & Binggeli 1994). NGC 205 was resolved into stars and thus confirmed as a Local Group member by Walter Baade, using the 100-inch telescope at Mount Wilson Observatory (Baade 1944a). He correctly identified NGC 205, at a projected distance of only 37 arcmin from M31, as a diffuse stellar system with a stellar population very much like that

of the Galactic globular clusters. NGC 147 and 185 form a close pair, separated by only 58 arcmin on the sky (van den Bergh 1998) and located some 7° away from M31. Baade confirmed NGC 147 and 185 as members of the Local Group by resolving them into individual stars (Baade 1944b). No new Local Group dEs have been discovered since then, while the census of the Local Group dwarf spheroidals (dSph), which are even fainter (absolute *B*-band magnitude $M_B \geq -13$ mag) and more diffuse than dEs, is most likely not yet complete. Since Baade could resolve these dwarf galaxies at about the same magnitude as M31, he surmised that they should be at roughly the same distance as M31. More precise distance measurements have since then clarified the geometry of the M31 satellite galaxy system. Using the tip of the red giant branch (TRGB) distances measured by McConnachie et al. (2005), $D_{\text{NGC}147} = 675 \pm 27$ kpc, $D_{\text{NGC}185} = 616 \pm 26$ kpc, $D_{\text{NGC}205} = 824 \pm 27$ kpc, $D_{\text{M31}} = 785 \pm 25$ kpc, which are in good agreement with those presented by Lee, Freedman & Madore (1993) and Lee (1996), and the angular distances between the galaxies, the following picture emerges.

[★]Based on observations collected at the Observatoire de Haute-Provence.

[†]E-mail: sven.derijcke@UGent.be (SDR)

[‡]Postdoctoral Fellow of the Fund for Scientific Research – Flanders (Belgium)(F.W.O).

Using the distance moduli and the sources of photometric errors given by McConnachie et al. (2005), we find that NGC 147 and 185 are separated by 63 ± 33 kpc and the couple is situated 160 kpc in front of M31. For all practical purposes, we can therefore treat them as isolated stellar systems. NGC 205, on the other hand, is situated 48 ± 30 kpc behind M31.

In this paper, we present dynamical models for NGC 147, 185 and 205. In order to construct a mass model for the luminous matter, we use Two-Micron All-Sky Survey (2MASS) *J*-band images of these galaxies, downloaded from the NASA/IPAC Infrared Science Archive web site. These dwarf galaxies have complex star formation histories and show evidence for spatial variations of the stellar population, the most striking being the very blue nucleus of NGC 205 (Peletier 1993; Han et al. 1997; Butler & Martínez-Delgado 2005). Therefore, the density distribution obtained from near-infrared *J*-band images should trace the mass distribution of the luminous matter more closely than that obtained from optical images. We measured the surface-brightness profile, position angle and ellipticity $\epsilon = 1 - b/a$ of all the three galaxies as a function of the geometric mean of major- and minor-axis distance, denoted by a and b , respectively. These were obtained using our own software. Basically, the code fits an ellipse through a set of positions where a given surface-brightness level is reached. The shape of an isophote, relative to the best-fitting ellipse with semimajor axis a and ellipticity ϵ , is quantified by expanding the intensity variation along this ellipse in a fourth-order Fourier series with coefficients S_4 , S_3 , C_4 and C_3 :

$$I(a, \theta) = I_0(a) [1 + C_3(a) \cos(3\theta) + C_4(a) \cos(4\theta) + S_3(a) \sin(3\theta) + S_4(a) \sin(4\theta)]. \quad (1)$$

Here, $I_0(a)$ is the average intensity of the isophote, and the angle θ is measured from the major axis. Using all photometric parameters, evaluated as a function of a , a smooth image of each galaxy is reconstructed. We used this smooth image to measure the total *J*-band magnitude and half-light radii. In each case, the total apparent magnitude we derive is within 0.05 mag of that listed in the 2MASS Large Galaxy Atlas (Jarrett et al. 2003). As to the half-light radii, we find for NGC 205 that $R_e(\text{NGC 205}) = 130$ arcsec (0.52 kpc), for NGC 147 that $R_e(\text{NGC 147}) = 122$ arcsec (0.38 kpc) and for NGC 185 that $R_e(\text{NGC 185}) = 90$ arcsec (0.27 kpc).

This smooth image is then deprojected in order to obtain the spatial density distribution of the stars. The spatial density of an axisymmetric stellar system cannot uniquely be reconstructed from the observed projected density if it is not viewed edge-on (Gerhard & Binney 1996). From the infinity of equally plausible positive, axially symmetric spatial densities that project to the observed projected density, we pick the one that can be represented as a weighted sum of basis functions, $\rho(\varpi, z) = \sum_k c_k \rho_k(\varpi, z)$, with $\rho_k(\varpi, z)$ of the form

$$\rho_k(\varpi, z) = \exp \left[- \left(\frac{\sqrt{\varpi^2 + (z/q_k)^2}}{\sigma_k} \right)^{m_k} \right]. \quad (2)$$

Here, σ_k is a scale radius, m_k is a shape parameter, making the density profile more (small m_k) or less (large m_k) centrally concentrated, q is the axis ratio, controlling the flattening of the basis function. These basis functions produce elliptical isophotes when projected on to the sky. For a given inclination, the unknown coefficients in the expansion of the spatial density are determined by fitting the projected basis functions to the observed photometry, evaluated on an elliptical, logarithmically spaced grid subject to the constraint that the spatial density is positive everywhere using a Quadratic

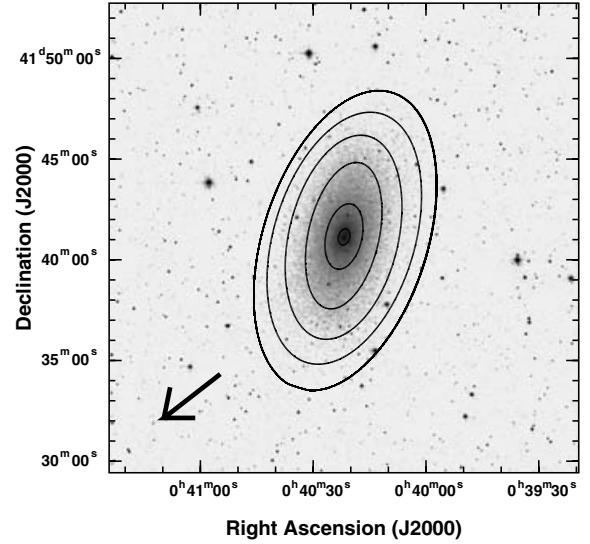


Figure 1. 2MASS *J*-band image of NGC 205. Overplotted on to this image are the fitted elliptical isophotes at *J*-band surface-brightness levels of 18, 19, 20, 21, 22 and 23 mag arcsec⁻². Beyond a major-axis distance of ≈ 300 arcsec, the isophotes of NGC 205 start to twist, by almost 10° between the 21 and 23 mag arcsec⁻² isophotes. The direction towards the centre of M31 is indicated by an arrow.

Programming algorithm (Dejonghe 1989). Note that the coefficients c_k can be negative, as long as the weighted sum of basis functions is positive. This algorithm has a library at its disposal that contains hundreds of basis functions to choose from. Typically, the χ^2 does not further improve after co-adding a few tens of components, and the procedure can be stopped. This deprojection procedure ensures that the spatial density is smooth, well behaved and positive.

Already from the 2MASS image, it is obvious that NGC 205 is noticeably influenced by the tidal forces exerted by M31 (see Fig. 1). Beyond a major-axis distance of ≈ 300 arcsec, the isophotes of NGC 205 twist from a position angle of 167° to 160° at 400 arcsec. At that radius, the surface-brightness profile also shows a downwards break, as can clearly be seen in Fig. 4, later (see also Hodge 1973; Choi, Guhathakurta & Johnston 2002). In these outer regions, peculiar kinematics, such as the outermost stars moving counter to the rotation of the main body (Geha et al. 2006), provide further evidence for a tidal interaction with M31. We will therefore check if our results for NGC 205 are affected by it being so close to M31. The isophotes of NGC 147 and 185 are much more regular, with negligible isophote twisting (see Figs 2 and 3).

The spectra were obtained with the 1.93-m telescope of the Observatoire de Haute-Provence, equipped with the CARELEC long-slit spectrograph. In combination with a EEV receptor with 2048×780 pixels of $15 \mu\text{m}$, the instrumental velocity dispersion was $\approx 25 \text{ km s}^{-1}$ ($R = 5050$) for a slit width of 1.5 arcsec. More details and a log of the observations can be found in Simien & Prugniel (2002). 10-min exposures on blank fields of sky obtained during the same night as the science exposures were used for sky subtraction. With a Fourier-Fitting technique (Franx, Illingworth & Heckman 1989), the spectrum of a G8III template star (HD5395), convolved with a Gaussian line-of-sight velocity distribution, yielded a good fit to the galaxy spectrum in Fourier space, providing a simultaneous estimate of the mean streaming velocity v_p and the projected velocity dispersion σ_p .

From the deep major-axis spectrum of NGC 205, stellar kinematics out to about 300 arcsec (1.2 kpc or 2.3 half-light radii)

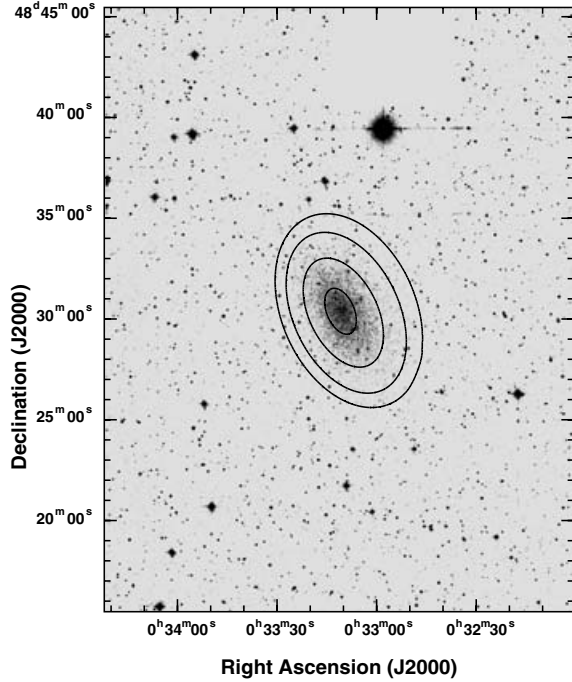


Figure 2. 2MASS *J*-band image of NGC 147. Overplotted on to this image are the fitted elliptical isophotes at *J*-band surface-brightness levels of 20, 21, 22 and 23 mag arcsec⁻².

could be extracted. The minor-axis spectra yield useful kinematic information out to 120 arcsec (0.9 kpc). Thanks to the proximity of this galaxy and the unprecedented depth of the spectra, we can measure kinematics near the centre of NGC 205 with a spatial resolution of ~ 5 –10 parsec. The major-axis spectrum of NGC 185 allows extracting kinematics out to ~ 100 arcsec (0.3 kpc or $1.1R_e$). NGC 147 has the lowest surface brightness of all Local Group dEs and is, moreover, riddled with foreground stars; and therefore it was the most difficult object to obtain decent kinematics for. The spectra of NGC 147 secured by Simien & Prugniel (2002) turned out to be insufficiently deep. We therefore reobserved NGC 147 in

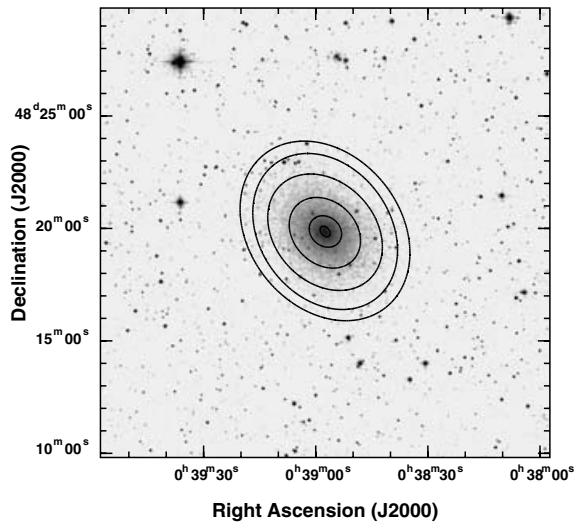


Figure 3. 2MASS *J*-band image of NGC 185. Overplotted on to this image are the fitted elliptical isophotes at *J*-band surface-brightness levels of 18, 19, 20, 21, 22 and 23 mag arcsec⁻².

2002 January and 2003 January using the same instrumental setup and the same data reduction procedure. With the addition of these new exposures (six 1-h exposures along the southern semimajor axis and four 1-h exposures along the northern semimajor axis), the major-axis kinematics of NGC 147 now extend out to ~ 150 arcsec (0.5 kpc or $1.2R_e$) along the northern semimajor axis and out to ~ 100 arcsec (0.3 kpc or $0.8R_e$) along the southern semimajor axis.

The details of the modelling method are given in Section 2. We present the results for each of the galaxies in Section 3. Our conclusions are summarized in Section 4.

2 THREE-INTEGRAL DYNAMICAL MODELS

The internal dynamics of a steady-state oblate stellar system are described by a gravitational potential $\psi(\varpi, z)$ that determines the stellar orbits, and the distribution function (DF) $F(\mathbf{r}, \mathbf{v}) d\mathbf{r} d\mathbf{v}$, which gives the number density of stars in phase space [(ϖ, z) are cylindrical coordinates in each meridional plane]. Loosely speaking, the DF distributes the stars over all possible orbits in a given potential. In the following, we will work in prolate elliptical coordinates (λ, ν) (Dejonghe & de Zeeuw 1988), defined by

$$\varpi^2 = \frac{(\lambda + \alpha)(\nu + \alpha)}{\alpha - \gamma}, \quad z^2 = \frac{(\lambda + \gamma)(\nu + \gamma)}{\gamma - \alpha}, \quad (3)$$

with $-\gamma \leq \nu \leq -\alpha \leq \lambda$. Surfaces of constant λ are confocal prolate spheroids; surfaces defined by constant ν are confocal two-sheeted hyperboloids, both with foci at $z = \pm \Delta = \pm \sqrt{\gamma - \alpha}$. We will approximate the gravitational potential by a Stäckel potential, of the form

$$\psi(\varpi, z) = \frac{(\lambda + \gamma)G(\lambda) - (\nu + \gamma)G(\nu)}{\lambda - \nu}, \quad (4)$$

with $G(\lambda)$ the potential in the equatorial plane. Such potentials allow the existence of three integrals of motion: the binding energy E , the z -component of the angular momentum L_z , which we use in the more convenient form $I_2 = L_z^2/2$, and

$$I_3 = \frac{1}{2}(L^2 - L_z^2) + (\gamma - \alpha) \left[\frac{1}{2}v_z^2 - z^2 \frac{G(\lambda) - G(\nu)}{\lambda - \nu} \right], \quad (5)$$

an integral which is a generalization of angular momentum conservation in spherical systems. Roughly, for a given E and I_2 , I_3 determines how high above the equatorial plane an orbit will come. Models that make use of the third integral are called three-integral or 3I models, versus two-integral or 2I models that go without it.

A detailed account of the method we employed to construct the spheroidal coordinate system and Stäckel potential that gives the best fit to a given axisymmetric potential can be found in Dejonghe & de Zeeuw (1988), Dejonghe et al. (1996) and De Bruyne et al. (2001). In brief, we deproject the observed surface-brightness distribution, derived from a 2MASS *J*-band image, assuming the galaxy to be axisymmetric. Since NGC 147 and 205 have a fairly flattened apparent shape, with an apparent axial ratio $q_{\text{app}} = 0.5$, it is quite unlikely that they are viewed far from edge-on. The intrinsic flattening distribution of dEs peaks around an intrinsic axial ratio $q_{\text{intr}} = 0.6$ while galaxies with an intrinsic axial ratio smaller than $q_{\text{intr}} = 0.4$ are virtually absent (Binggeli & Popescu 1995). Assuming both galaxies to have an oblate, axisymmetric light distribution that is intrinsically rounder than a $q_{\text{intr}} = 0.4$ shape, the inclination is expected to be larger than $i \sim 70^\circ$. Therefore, we can assume for simplicity that NGC 147 and 205 are viewed edge-on without significantly affecting any of the results. NGC 185, on the other hand, has a much rounder apparent shape, with an apparent axial ratio $q_{\text{app}} = 0.8$. If we assume that the galaxy has an intrinsic shape that

is rounder than $q_{\text{intr}} = 0.4$, the inclination is expected to be larger than $i \sim 40^\circ$. In order to assess the influence of the intrinsic shape and the viewing angle of NGC 185 on our results, we generated models with $i = 90^\circ, 60^\circ, 55^\circ, 50^\circ$ and 45° . However, with kinematics along the major axis only and lacking higher order moments of the line-of-sight velocity distribution, the kinematical data do not allow to constrain the inclination with any degree of precision.

The total mass density, including dark matter, is parametrized as the spatial luminous mass density multiplied by a spatially varying mass-to-light ratio

$$\frac{M}{L}(\varpi, z) = A(1 + B\sqrt{\varpi^2 + (z/q)^2}), \quad (6)$$

with the parameters A and B to be estimated from the data and q the axis ratio of the luminosity density distribution. Attempts to find intermediate-mass black holes in dEs, using either ground-based kinematics (Geha, Guhathakurta & van der Marel 2002) or high spatial resolution kinematical information obtained with *Hubble Space Telescope* (HST) (Valluri et al. 2005), have so far failed. For this reason, and since we are mostly interested in the total dark-matter content of these galaxies, we did not include a central black hole in our models. The gravitational potential is obtained by decomposing the total mass density in spherical harmonics. Finally, we determine the Stäckel potential, i.e. the focal length Δ and the function G , that best fits this gravitational potential. The Stäckel form of the potential is used only to calculate the third integral I_3 ; elsewhere the potential derived from spherical harmonics is used. The potential is normalized such that $\psi(r) = 1/r$ at large radius r , with r expressed in kiloparsec.

For a given potential, we wish to find the DF that best reproduces the kinematical information. As a first step, the DF is written as a weighted sum of basis functions, called ‘components’. Here, we will use components of the form

$$F^{i, \epsilon_i}(E, I_2, I_3) = (E - E_{0,i})^{\sigma_i} (I_2 - I_{0,i})^{\tau_i} I_3^{\rho_i}, \quad \text{if } E > E_{0,i}, \epsilon_i I_2 > I_{0,i} \geq 0$$

$$= 0, \quad \text{if } E \leq E_{0,i} \text{ or } \epsilon_i I_2 \leq I_{0,i} \quad (7)$$

with σ_i, τ_i and ρ_i integer numbers. $E_{0,i}$ is a lower bound on the binding energy, which defines the outer boundary within which the component is non-zero. The parameter ϵ_i indicates whether stars are placed only on orbits with positive angular momentum ($\epsilon_i = +1$) or only on orbits with negative angular momentum ($\epsilon_i = -1$) or on both ($\epsilon_i = 0$). We refer the reader to Appendix A for a discussion of the properties of these components. The DF then takes the form $F(E, I_2, I_3) = \sum_i c_i F^{i, \epsilon_i}(E, I_2, I_3)$. The coefficients c_i are determined by minimizing the quantity

$$\chi^2 = \sum_l \left(\frac{\text{obs}_l - \sum_i c_i \text{obs}_l^i}{\sigma_l} \right)^2, \quad (8)$$

with obs_l an observed data point, σ_l the 1σ error bar on that data point and obs_l^i the corresponding value calculated from the basis function F^{i, ϵ_i} , subject to the constraint that the DF be positive everywhere in phase space. Note that the coefficients c_i can be negative, as long as the weighted sum of basis functions is positive.

The projected velocity moments, $\mu_n(\Omega)$, can be obtained by integrating suitably weighted combinations of the spatial velocity moments over a line of sight in a direction Ω :

$$\mu_n(\Omega) = \int_{\Omega} v_p^n F(E, I_2, I_3) dv d\xi$$

$$= \sum_i c_i \int_{\Omega} v_p^n F^{i, \epsilon_i}(E, I_2, I_3) dv d\xi \quad (9)$$

with v_p the line-of-sight velocity and ξ a coordinate along the line of sight. From the observed quantities, the projected luminosity density $\rho_p = 10^{(25.26 - \mu_J)/2.5} L_{J, \odot} \text{pc}^{-2}$ with μ_J the observed surface brightness expressed in magnitude arcsec^{-2} , the mean projected velocity v_p and the projected velocity dispersion σ_p , one can easily construct observed values for the lowest order velocity moments $\mu_0 = \rho_p$, $\mu_1 = \rho_p v_p$ and $\mu_2 = \rho_p (v_p^2 + \sigma_p^2)$ along each observed line of sight and insert these values into equation (8), which is minimized using a Quadratic Programming algorithm (Dejonghe 1989). The minimization algorithm has a library at its disposal that contains hundreds of components to choose from. Since the algorithm itself determines which and how many components are used, this is a virtually non-parametric method of retrieving the DF. Typically, the χ^2 does not further improve after co-adding a few tens of components, and the procedure can be stopped. This finally yields the coefficients c_i and consequently the DF that best reproduces the data for a given gravitational potential. If the basis functions F^{i, ϵ_i} are smooth and well-behaved functions of the integrals of motion, any combination of a finite number of basis functions will by construction also be smooth and well behaved in phase space.

It is well known that in a spherical geometry even complete kinematical knowledge does not suffice to uniquely constrain both the gravitational potential and the DF. On the contrary: for each potential, there is a unique DF that reproduces the data (Dejonghe & Merritt 1992). That DF, however, need not be positive everywhere in phase space. The positivity constraint we are imposing on the DF therefore helps to constrain the gravitational potential. The degeneracy in the general axisymmetric case, however, can be expected to be a lot smaller than in the spherical case. For 2I models, the even part of the DF can be derived directly from the augmented stellar density $\tilde{\rho}(\varpi, \psi)$ which, in the absence of dark matter, can in principle be constructed directly by deprojecting the observed surface-brightness distribution. This is clearly not possible in the spherical case. Therefore, even if the kinematical data are restricted to the three lowest order moments of the DF along the major (and sometimes minor) axis, we can expect to be able to put meaningful constraints on the dark-matter content and mass, a point already made in Dejonghe et al. (1996). 3I models have a larger freedom in distributing stars over all possible orbits than 2I models, widening somewhat the range of possible solutions that is consistent with the data.

We fitted models to the data of each galaxy with various values for the parameters A and B in equation (6). The model with the lowest χ^2 value, which most closely reproduces the data, is retained as the best model. The uncertainties on the dynamical quantities presented in this paper are derived from the range of allowed models (all models within the 95 per cent confidence level are deemed acceptable).

3 RESULTS

3.1 NGC 205

3.1.1 New and previous kinematical work

The major- and minor-axis J -band photometry and kinematics of NGC 205 as measured by Simien & Prugniel (2002) are presented in Fig. 4. These data were derived from spectra with a 25 km s^{-1} velocity resolution, using a Fourier-Fitting technique. Detailed simulations showed that template mismatch has little effect on the kinematical parameters (Koleva et al. 2006). There is a slight degeneracy between the velocity dispersion and the metallicity: a template of too high a metallicity will give too large a dispersion. The template

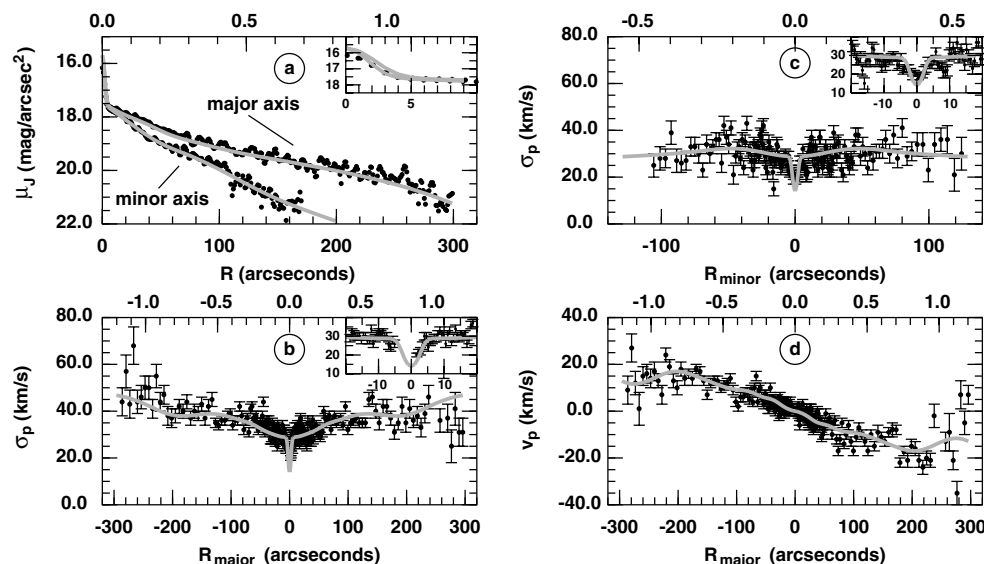


Figure 4. Fit to the kinematics of NGC 205. Panel (a): the J -band surface brightness, μ_J , along major and minor axis; panel (b): the major-axis velocity dispersion, σ_p ; panel (c): the minor-axis velocity dispersion; panel (d): the mean streaming velocity along the major axis, v_p . The black dots are the data points, the grey curves correspond to the best-fitting dynamical model. The top axis of each panel is labelled with radius expressed in kiloparsec. The model was fitted to the surface brightness on a logarithmically spaced grid covering the whole face of the galaxy, but for clarity we only plot the major- and minor-axis profiles in this figure. The model accurately reproduces the central surface-brightness peak (see insets in panel a), and the corresponding central drop in the velocity dispersion (see insets in panels b and c). The major-axis velocity dispersion appears to keep rising very slowly out to the last data point, at 5 arcmin.

star we used has a metallicity $[\text{Fe}/\text{H}] = -0.5$ (Prugniel & Soubiran 2001). Our simulations show that for a galaxy with $[\text{Fe}/\text{H}] = -1$ and a template with $[\text{Fe}/\text{H}] = -0.5$, the dispersion can be overestimated by ~ 12 per cent at most. However, the fitting procedure includes an additive continuum which decreases the mismatch by an order of magnitude. Age mismatch, as is likely to be the case in the peculiar nucleus of NGC 205, is not expected to bias the kinematics.

NGC 205 has a very steep central density cusp or nucleus (see panel a of Fig. 4). Within the inner 3 arcsec, the J -band surface brightness becomes almost $2 \text{ mag arcsec}^{-2}$ brighter. This sudden density jump is reflected in a corresponding drop of the velocity dispersion by about 10 km s^{-1} towards the centre; from $\sigma_p = 30 \pm 2 \text{ km s}^{-1}$ at a radius of 10 arcsec down to a central velocity dispersion of $\sigma_p = 20 \pm 1 \text{ km s}^{-1}$ (see panels b and c of Fig. 4). The nucleus of NGC 205 therefore appears to be a round and very dense but dynamically cold substructure. Outside the nucleus, the velocity dispersion was found to rise outwardly from $30 \pm 2 \text{ km s}^{-1}$ near the centre up to about $45 \pm 7 \text{ km s}^{-1}$ at 300 arcsec. The rotation velocity rises to a maximum of $20 \pm 5 \text{ km s}^{-1}$ at 200 arcsec and declines again beyond that radius. This was the first clear detection of rotation in this galaxy. There is evidence that the mean velocity reverses sign at a radius of about 300 arcsec. This feature agrees with other observations (Hodge 1973; Geha et al. 2006) that suggest that the tidal forces of M31 only appreciably affect the outer regions of NGC 205, beyond 5 arcmin. Moreover, the absence of minor-axis rotation (Simien & Prugniel 2002) and the presence of a very dense nucleus, which is likely to scatter stars off box orbits, which are the backbone of any slowly rotating triaxial mass distribution, into loop orbits (Evans & Collett 1994; Merritt & Quinlan 1998) both argue against NGC 205 having a strongly triaxial mass distribution, justifying our assumption of an oblate geometry for the construction of dynamical models.

Previous work on the kinematics of NGC 205 has yielded contradictory results. Held, Mould & de Zeeuw (1990) present major-axis velocity and velocity dispersion profiles out to about 1 arcmin, mea-

sured from spectra with a 83 km s^{-1} per pixel spectral resolution and using a G5 star spectrum as template. The mean velocity dispersion is about $60\text{--}70 \text{ km s}^{-1}$, with only a very slight decline towards the centre, reaching about 50 km s^{-1} in the very centre. No significant rotation was detected. These authors deduce a mass-to-light ratio of $(M/L)_B \sim 7 M_\odot/L_{\odot,B}$. Bender, Paquet & Nieto (1991), on the other hand, found the velocity dispersion to rise almost linearly with radius, from $\sim 30 \text{ km s}^{-1}$ near the centre to $\sim 70 \text{ km s}^{-1}$ at one half-light radius. At the very centre, the velocity dispersion was found to drop to 20 km s^{-1} . Again, rotation turned out to be negligible. The kinematics were derived at a 30 km s^{-1} spectral resolution using a single G8III stellar template spectrum. These authors estimate the B -band mass-to-light ratio at $(M/L)_B = 8 \pm 2 M_\odot/L_{\odot,B}$. In Held et al. (1992), the mean value of the major-axis velocity dispersion of NGC 205, $\langle \sigma \rangle = 42 \text{ km s}^{-1}$, is used to arrive at $(M/L)_B \sim 3.5 M_\odot/L_{\odot,B}$. Carter & Sadler (1990), on the other hand, retrieved an almost flat velocity dispersion out to 1 arcmin, constant at about 45 km s^{-1} . Very near the centre, the velocity dispersion was observed to drop to $\sim 15 \text{ km s}^{-1}$. These kinematics were measured using a composite stellar template from a galaxy spectrum with a very high spectral resolution (5 km s^{-1}). These authors estimate the mass-to-light ratio at $(M/L)_B \sim 9.4 M_\odot/L_{\odot,B}$ with an uncertainty of a factor of 2.

3.1.2 The dynamical mass and mass-to-light ratio

From the range of models that is compatible with the data at the 95 per cent confidence level (see Fig. 5), we estimate the mass within a $2R_e$ radius sphere at $M(2R_e) = 10.2^{+3.3}_{-2.2} \times 10^8 M_\odot$, corresponding to a J -band mass-to-light ratio within the inner $2R_e$ of $(M/L)_J = 2.2^{+0.7}_{-0.4} M_\odot/L_{\odot,J}$ or a B -band mass-to-light ratio of $(M/L)_B = 4.5^{+1.5}_{-1.0} M_\odot/L_{\odot,B}$, using a $B - J = 2.397$ colour, corrected for Galactic reddening (de Vaucouleurs et al. 1991; Jarrett et al. 2003). The mean metallicity of NGC 205 is quite well determined at $[\text{Fe}/\text{H}] \approx -0.9$, using various techniques (Richer, McCall &

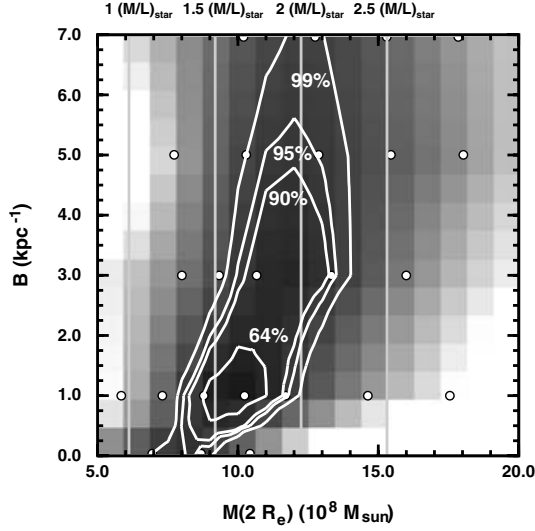


Figure 5. Contours of constant χ^2 for the models fitted to the NGC 205 data as a function of the total mass within a $2R_e$ radius, $M(2R_e)$, and the scale parameter B of equation (6). The white dots mark the parameter values of the models we constructed. The contours indicate the 64, 90, 95 and 99 per cent confidence levels. At the 95 per cent confidence level, the mass within a $2R_e$ radius is $M(2R_e) = 10.2^{+3.3}_{-2.2} \times 10^8 M_\odot$. For the scale parameter, we find $B = 1.1^{+4.5}_{-1.1} \text{ kpc}^{-1}$ at the same confidence level. The best-fitting model evidently requires a spatially varying mass-to-light ratio to reproduce the data. Models with a constant mass-to-light ratio, i.e. with $B = 0 \text{ kpc}^{-1}$, are barely acceptable at the 95 per cent confidence level. The vertical lines indicate the locus of models for which the mass-to-light ratio at $2R_e$ equals 1, 1.5, 2 and 2.5 times the estimated stellar mass-to-light ratio $[(M/L)_J = 1.32]$; see Section 3.1.2]. All acceptable models, even the ones with a zero B , have mass-to-light ratios well above that of a purely stellar system.

Stasińska 1998; Butler & Martínez-Delgado 2005; McConnachie et al. 2005). In the central regions of our dynamical models, mass follows light. If the central mass-to-light ratio of the best-fitting model, $(M/L)_J = 1.32 M_\odot/L_\odot$, is indicative of that of the stel-

lar population and if we adopt a mean metallicity $[\text{Fe}/\text{H}] \approx -0.9$, we estimate the mean age of the stellar population at ~ 9 Gyr (Worthey 1994), which is not unreasonable. The model with the lowest mass that is still consistent with the data at the 95 per cent confidence level has a constant mass-to-light ratio $(M/L)_J = 1.8 M_\odot/L_\odot$, which is significantly higher than that estimated for the stellar population above. Hence, we can state that NGC 205 is *not* a pure stellar system, completely devoid of dark matter. Within a $2R_e$ sphere, NGC 205 consists of about 60 per cent luminous matter, by mass, and of 40 per cent dark matter.

3.1.3 The internal dynamics

The best-fitting 3I model for NGC 205 very accurately reproduces the photometric and kinematical data, as can be judged from Fig. 5, where the kinematics of the best-fitting model are overplotted on to the data. Since the dynamics of this galaxy are constrained by kinematical information along both the major and the minor axes, it is instructive to more closely examine some internal dynamical quantities. In Fig. 6, the spatial kinematics are presented in the meridional plane: the radial velocity dispersion σ_r , the tangential velocity dispersion σ_ϕ , the difference between the radial and vertical velocity dispersions $\sigma_r - \sigma_z$ (in the case of a 2I model: $\sigma_r - \sigma_z = 0$) and the mean tangential velocity v_ϕ .

Geometrically, it is clear that the minor-axis velocity dispersion puts strong constraints on the behaviour of the radial velocity dispersion along the symmetry axis while the major-axis kinematics constrain both the radial and the tangential velocity dispersion within the equatorial plane. The vertical velocity dispersion is only very weakly constrained by the kinematical data; it will mostly be determined by the photometry, i.e. by the flattening of the stellar distribution. As is clear from Figs 4, 6 and 7, the behaviour of the major-axis projected velocity is reflected in that of the tangential component σ_ϕ of the velocity dispersion tensor: the maximum around 0.5 kpc (125 arcsec) and the outward rise beyond 0.8 kpc (200 arcsec) can be clearly identified. The run of the radial velocity dispersion along the z -axis closely traces the minor-axis projected velocity dispersion, as

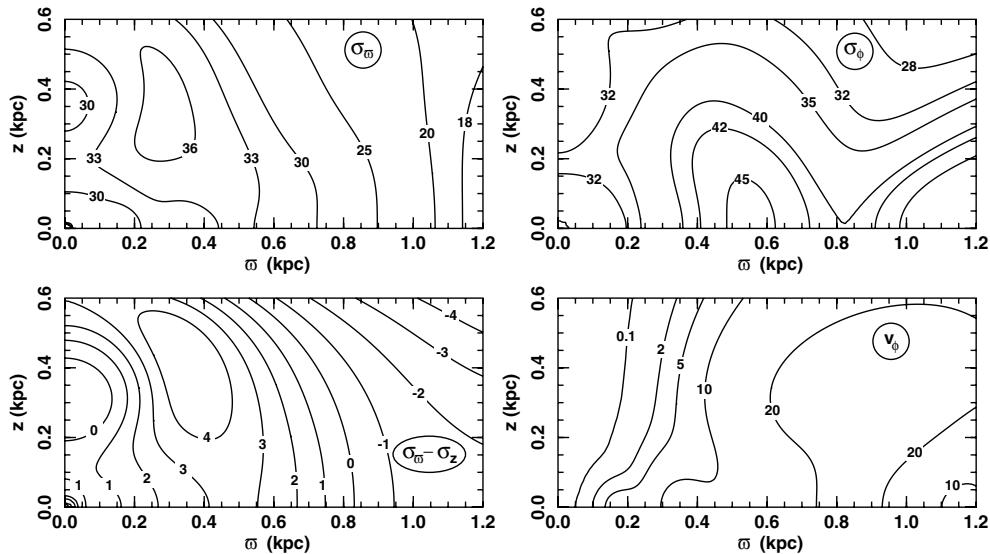


Figure 6. Contours for the radial velocity dispersion, σ_r , the tangential velocity dispersion, σ_ϕ , the difference between the radial and the vertical velocity dispersion, $\sigma_r - \sigma_z$, and the mean tangential velocity, v_ϕ , in the meridional plane of the best-fitting dynamical model for NGC 205. All contours are labelled in km s^{-1} .

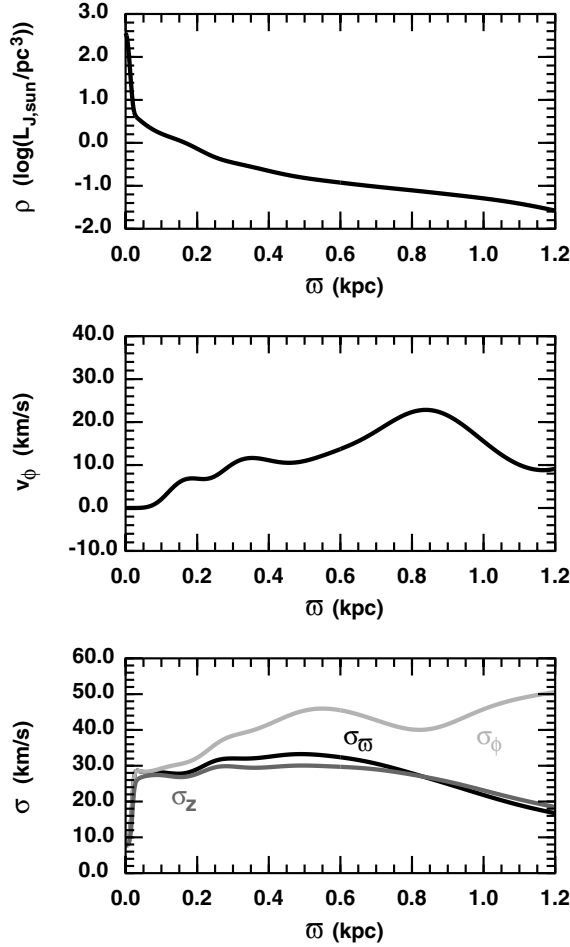


Figure 7. The internal dynamics of the best-fitting model for NGC 205, plotted as a function of radius within the equatorial plane. Top panel: the logarithm of the luminosity density of the stars, ρ ; middle panel: the rotation velocity, v_ϕ ; bottom panel: the radial, tangential and vertical components of the velocity dispersion tensor.

expected; cf. the maximum around 0.2 kpc (50 arcsec). In a 3I model, the radial and vertical velocity dispersions are decoupled. Still, the radial versus vertical anisotropy is very small: the vertical velocity dispersion is only marginally smaller than the radial dispersion within the inner 0.8 kpc (200 arcsec). If we use the anisotropy parameter $\beta_{\varpi,z} = 1 - (\sigma_z/\sigma_\varpi)^2$ to quantify this anisotropy, then we find that $-0.6 < \beta_{\varpi,z} < 0.3$ everywhere in the meridional plane. The radial versus tangential anisotropy is somewhat larger. If we introduce the quantity $\beta_{\varpi,\phi} = 1 - (\sigma_\phi/\sigma_\varpi)^2$, then we find that $-1 < \beta_{\varpi,\phi} < 0.1$ within the region that is well constrained by the kinematical data. Beyond a radius of 0.8 kpc, the tangential anisotropy increases to keep up with the observed rise of the projected velocity dispersion along the major axis.

The mean tangential velocity v_ϕ rises only very slowly as a function of radius, as does the projected mean velocity v_p along the major axis. The velocity reaches a maximum at 0.8 kpc (200 arcsec) and declines beyond that radius (see Fig. 7). Extrapolating somewhat beyond the extent of our data, the velocity is expected to reverse sign at about 300 arcsec, in agreement with Geha et al. (2006). From Fig. 8, it is clear that there is only a slight excess of stars with positive angular momentum L_z causing the observed rotation. Only beyond ~ 0.7 kpc does the number of stars with $L_z > 0$ clearly

dominate that of $L_z < 0$ stars. At a radius of ~ 1 kpc, there are about twice as many stars on right-handed near-circular orbits as there are on left-handed ones.

NGC 205 has a very distinct nucleus, which shows up in the dynamical model as a spherically symmetric, dynamically very cold substructure (see Figs 6 and 7). By singling out those basis functions for the DF that makes up the nucleus, i.e. the basis functions with a very small outer boundary, we can study the nucleus in more detail. The nucleus can be modelled as an isotropic star cluster with a one-dimensional velocity dispersion $\sigma \approx 7 \text{ km s}^{-1}$ and a truncation radius of about 50 pc. By integrating the spherically symmetric mass density of the nucleus, we estimate its total mass at $1.4 \times 10^6 M_\odot$. This is in excellent agreement with a previous estimate based on a King model fit to the surface-brightness profile of the nucleus and its projected velocity dispersion (Carter & Sadler 1990; Jones et al. 1996). It should be noted, however, that the mass-to-light ratio of the nucleus is probably different from that of the main body of NGC 205 (Valluri et al. 2005). The functional form for the mass-to-light ratio adopted by us, equation (6), cannot reproduce a central M/L variation. However, this is not our intention: we are interested in quantifying the amount of dark matter at large radii. Since the nucleus contributes only of the order of 0.1 per cent of the total mass of the galaxy, our total mass estimates are robust.

Thus, the nucleus of NGC 205 is structurally and dynamically not unlike a massive globular cluster. The orbital decay time-scale for a globular cluster in NGC 205 by dynamical friction is of the order of 10^8 – 10^9 yr, significantly less than a Hubble time (Tremaine, Ostriker & Spitzer 1975; Jones et al. 1996; Lotz et al. 2001), which makes it plausible that one or more star clusters have spiralled inwards and settled at the bottom of the gravitational well. Though detailed N -body simulations of this process are still lacking, the observed properties of the NGC 205 nucleus are not inconsistent with this scenario.

3.1.4 The tidal influence of M31

The TRGB distance estimates from McConnachie et al. (2005) place NGC 205 48 ± 33 kpc behind M31. The 1σ error on the TRGB estimates for the distances of NGC 205 and M31 is large enough that it is quite plausible that NGC 205 and M31 are at the same distance from the Milky Way and hence at a relative distance of a mere 10 kpc.

In order to get a rough estimate of how the presence of M31 affects our results, we approximate the gravitational potential of M31 as that of a spherical mass distribution at a distance R from NGC 205. For computational ease, we will further assume that the centre of mass of M31 lies within the equatorial plane of NGC 205 and that distances within the stellar body of NGC 205 are much smaller than R . We then axisymmetrize this potential by averaging it over the azimuthal angle ϕ . We finally obtain the expression

$$\Phi_{\text{tidal,M31}}(\varpi, z) = -\frac{GM(R)}{\varpi} \left[\frac{1}{4} \left(\frac{\varpi}{R} \right)^2 - \frac{1}{2} \left(\frac{z}{R} \right)^2 + \frac{9}{64} \left(\frac{\varpi}{R} \right)^4 - \frac{9}{8} \left(\frac{\varpi}{R} \right)^2 \left(\frac{z}{R} \right)^2 + \frac{3}{8} \left(\frac{z}{R} \right)^4 + \mathcal{O}(6) \right] \quad (10)$$

for the axisymmetric potential corresponding to the tidal field of M31, up to fourth order in z/R and ϖ/R , with $M(R)$ the mass of M31 enclosed within a sphere of radius R (Klypin, Zhao & Somerville 2002).

We plot the gravitational potential of the best-fitting dynamical model for NGC 205 as a function of radius in the equatorial plane. The top curve is the potential of the model in the absence of M31.

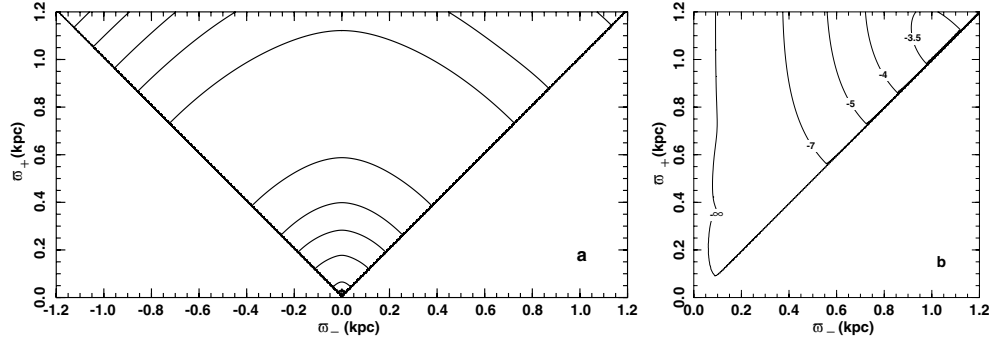


Figure 8. Panel (a): the DF of the best-fitting dynamical model for NGC 205, plotted in turning-point space for loop orbits in the equatorial plane, characterized by $I_3 = 0$. The pericentre distance is denoted by w_- ; the apocentre distance by w_+ . Radial orbits populate the $w_- = 0$ axis while circular orbits lie along the diagonal. w_- has the same sign as the angular momentum L_z . The contour labels are expressed in units of $\log [L_{\odot, J} \text{ pc}^{-3} (50 \text{ km s}^{-1})^{-3}]$, from -4.5 to 1.0 with a 0.5 interval. The orbital distribution within the equatorial plane is clearly very nearly isotropic, with only a very slight excess of stars with positive angular momentum L_z , causing the rotation of NGC 205. Panel (b): to have a more detailed look at this slight excess of stars on positive angular momentum orbits, we plotted $F(E, L_z > 0, 0) - F(E, L_z < 0, 0)$. The contour labels are expressed in units of $\log [L_{\odot, J} \text{ pc}^{-3} (50 \text{ km s}^{-1})^{-3}]$. At small radii, there is almost exact counter rotation, with stars on positive and negative angular momentum orbits almost cancelling any rotation. At larger radii, the number of stars on positive angular momentum orbits starts to dominate, and at a radius of ~ 1 kpc, there are about twice as many stars on right-handed near-circular orbits as there are on left-handed ones.

From top to bottom, the other curves indicate the potential in the presence of the axisymmetrized tidal field of M31 for relative distances of 40, 20, 10 and 5 kpc between NGC 205 and M31. Even for the minimum current relative distance allowed by the observations, i.e. 10 kpc, the tidal influence of the giant spiral galaxy is negligible within the region for which we have kinematical data, that is within the inner 1.2 kpc. In that case, stars beyond 2.8 kpc (700 arcsec) are unbound. If NGC 205 has passed by M31 with a pericentric distance as small as 5 kpc, stars are unbound beyond a radius of ~ 1.5 kpc. These values can be compared with the analytical estimate

$$r_{\text{tidal}} \simeq r_{\text{peri}} \left(\frac{M_{\text{sat}}}{x M_{\text{gal}}} \right)^{1/3}, \quad (11)$$

with r_{peri} the orbital radius of a satellite galaxy with mass M_{sat} around a galaxy with mass M_{gal} , and $x = 9$ or 1 , for stars inside the satellite galaxy on prograde or retrograde circular orbits, respectively (Read et al. 2006). For a pericentric distance of 10 kpc, this yields $r_{\text{tidal}} = 1.0$ – 2.0 kpc (depending on x); for a pericentric distance of 5 kpc, this yields $r_{\text{tidal}} = 0.6$ to 1.3 kpc. We substituted the mass of M31 enclosed within a radius r_{peri} for M_{gal} . These are also the radii where in Fig. 9 the ‘effective’ potential starts to deviate significantly from that of NGC 205 alone. This makes us confident that we are providing an adequate description of the tidal influence of M31 on NGC 205.

Small pericentric distances, i.e. smaller than ~ 5 – 10 kpc, which may have occurred in the past, not only lead to a large effect on the force field within the inner 1.2 kpc but also give rise to a tidal radius well within the region constrained by the photometric and kinematical data, in which case the construction of equilibrium models itself becomes meaningless. In short, our results are robust if NGC 205 has kept a distance of at least ~ 10 kpc from M31.

3.2 NGC 147

3.2.1 New and previous kinematical work

The major- and minor-axis J -band photometry and the major-axis kinematics of NGC 147 as measured by Simien & Prugniel (2002), including the additional exposures obtained in 2002 January and 2003, are presented in Fig. 10. The kinematics of NGC 147 extend

out to ~ 150 arcsec (0.5 kpc or $0.8 R_e$). The projected velocity dispersion is roughly constant, at about $\sigma_p \approx 25 \text{ km s}^{-1}$. The rotation curve is consistent with NGC 147 having zero rotation. The velocity dispersion profile is in good agreement with the one presented by Bender et al. (1991). However, these authors found significant rotation in NGC 147, with an amplitude of $\sim 10 \text{ km s}^{-1}$ at a radius of 100 arcsec. They estimated the B -band mass-to-light ratio of NGC 147 at $(M/L)_B = 7 \pm 3 M_{\odot}/L_{\odot, B}$.

3.2.2 The dynamical mass and mass-to-light ratio

The total mass within a $2R_e$ radius sphere is estimated at $M(2R_e) = 3.0^{+2.4}_{-1.8} \times 10^8 M_{\odot}$, corresponding to a J -band mass-to-light

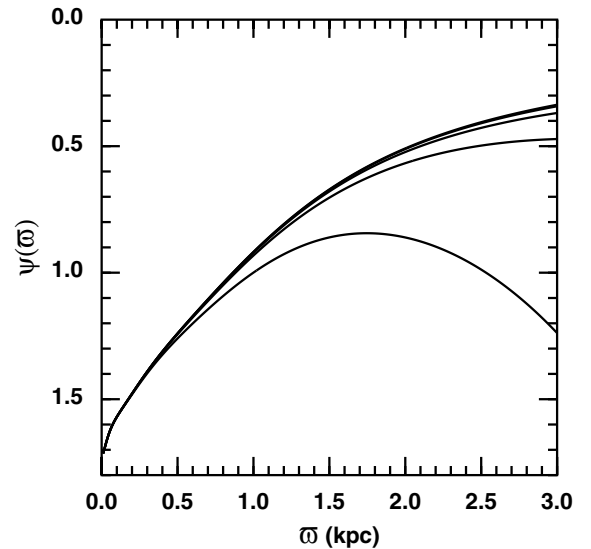


Figure 9. The gravitational potential well ψ of NGC 205 in the equatorial plane as a function of radius w . The top curve is the gravitational potential of the best-fitting dynamical model for NGC 205 in the absence of M31. From top to bottom, the other curves indicate the ‘effective’ potential in the presence of the axisymmetrized tidal field of M31 (equation 10) for relative distances of 40 (which essentially overlaps with the unperturbed potential of NGC 205), 20, 10 and 5 kpc between NGC 205 and M31.

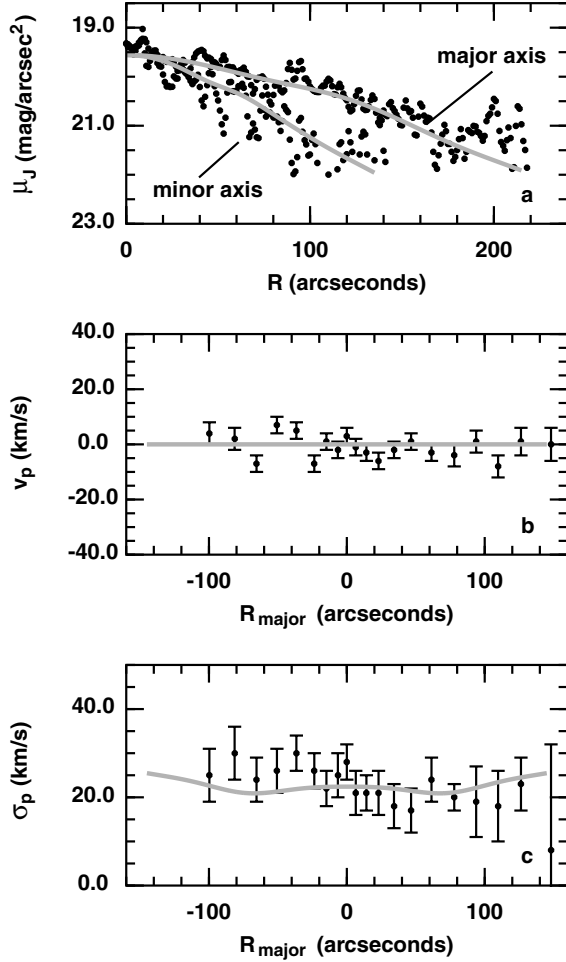


Figure 10. Fit to the kinematics of NGC 147. Panel (a): the J -band surface brightness, μ_J , along major and minor axis; panel (b): the mean streaming velocity along the major axis, v_p ; panel (c): the major-axis velocity dispersion, σ_p . The black dots are the data points, and the grey curves correspond to the best-fitting dynamical model. The model was fitted to the surface brightness on a grid covering the whole face of the galaxy, but for clarity we only plot the major- and minor-axis profiles in this figure. The major-axis velocity dispersion remains approximately constant at $\sigma_p \sim 25 \text{ km s}^{-1}$ out to the last data point, at 2.3 arcmin.

ratio within the inner $2R_e$ of $(M/L)_J = 3.4^{+2.7}_{-2.0} M_\odot/L_{\odot,J}$ or a B -band mass-to-light ratio of $(M/L)_B = 4.0^{+3.2}_{-2.4} M_\odot/L_{\odot,B}$. The mean metallicity of the stellar population is $[\text{Fe}/\text{H}] \approx -1.0$ (Han et al. 1997; McConnachie et al. 2005). There is no evidence that NGC 147 contains a population of intermediate-age stars (Renzini 1998); Mould, Kristian & Da Costa (1983) estimate that 90 per cent of the stellar population is older than 12 Gyr. Using 12 Gyr as a rough estimate for the mean age of the stellar population, the stellar mass-to-light ratio is $(M/L)_J \sim 1.6 M_\odot/L_{\odot,J}$ or $(M/L)_B \sim 2.6 M_\odot/L_{\odot,B}$ (Worthey 1994). Comparing this with the dynamical mass-to-light ratio of the best-fitting dynamical model, we find that NGC 147 consists of about 50 per cent luminous matter, by mass, and of 50 per cent dark matter.

3.2.3 The internal dynamics

The stellar density and the radial, tangential and vertical components of the velocity dispersion tensor of the best-fitting model for

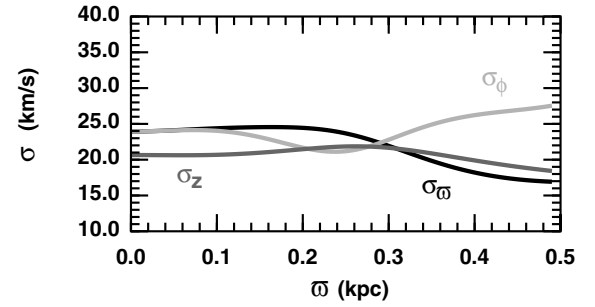


Figure 11. The radial, tangential and vertical components of the velocity dispersion tensor of the best-fitting model of NGC 147. All quantities are plotted as a function of radius within the equatorial plane. The spatial stellar density profile within the equatorial plane is consistent with being exponentially declining from a central density of $0.32 L_{J,\odot} \text{ pc}^{-3}$ with an exponential scale-length of 0.31 kpc.

NGC 147 are presented in Fig. 11. The velocity dispersion tensor is almost isotropic, with $\sigma \approx 20\text{--}25 \text{ km s}^{-1}$, up to a radius of 0.3 kpc, with the vertical velocity dispersion being somewhat lower to help flatten the galaxy. Outside 0.3 kpc, the tangential velocity dispersion rises up to $\sigma_\phi \approx 27 \text{ km s}^{-1}$ in sync with the projected velocity dispersion (Fig. 10).

3.3 NGC 185

3.3.1 New and previous kinematical work

The major- and minor-axis J -band photometry and major-axis kinematics of NGC 185 as measured by Simien & Prugniel (2002) are presented in Fig. 12. The kinematics of NGC 185 extend out to $\sim 100 \text{ arcsec}$ (0.3 kpc or $1.1R_e$). The major-axis velocity dispersion is roughly constant at about 30 km s^{-1} , in good agreement with Bender et al. (1991). There is a hint of rotation, at variance with Bender et al. (1991), but, as in the case of NGC 147, sky subtraction at these low surface-brightness levels is very difficult, and this might affect the measurements. Bender et al. (1991) estimate the B -band mass-to-light ratio of NGC 185 at $(M/L)_B = 5 \pm 2 M_\odot/L_{\odot,B}$. Held et al. (1992) found an essentially flat velocity dispersion profile, with $\sigma \approx 30 \text{ km s}^{-1}$. Interestingly, their major-axis velocity dispersion profile shows a central peak, with the dispersion rising to a central value of 50 km s^{-1} . These authors used a spherically symmetric, isotropic model with an exponentially declining density profile to estimate the central mass-to-light ratio of NGC 185 at $(M/L)_B \sim 3 M_\odot/L_{\odot,B}$.

3.3.2 The dynamical mass and mass-to-light ratio

The best-fitting model, with $i = 50^\circ$ and an intrinsic axial ratio $q_{\text{intr}} = 0.62$, yields our best estimate for the mass of NGC 185. The error bar on this quantity is estimated taking into account all inclination angles. We estimate the mass within a $2R_e$ radius sphere at $M(2R_e) = 2.6^{+0.8}_{-0.6} \times 10^8 M_\odot$, corresponding to a J -band mass-to-light ratio within the inner $2R_e$ of $(M/L)_J = 2.2^{+0.6}_{-0.5} M_\odot/L_{\odot,J}$ or a B -band mass-to-light ratio of $(M/L)_B = 3.0^{+1.0}_{-0.7} M_\odot/L_{\odot,B}$. This result is in good agreement with the one obtained by Held et al. (1992). The mean metallicity of the stellar population is estimated at $[\text{Fe}/\text{H}] = -1.43 \pm 0.15$ by Martínez-Delgado & Aparicio (1998). Lee et al. (1993) find NGC 185 to contain a complex stellar population with a mean metallicity of $[\text{Fe}/\text{H}] = -1.23 \pm 0.16$. McConnachie et al. (2005) derive a value $[\text{Fe}/\text{H}] = -1.2$. Using

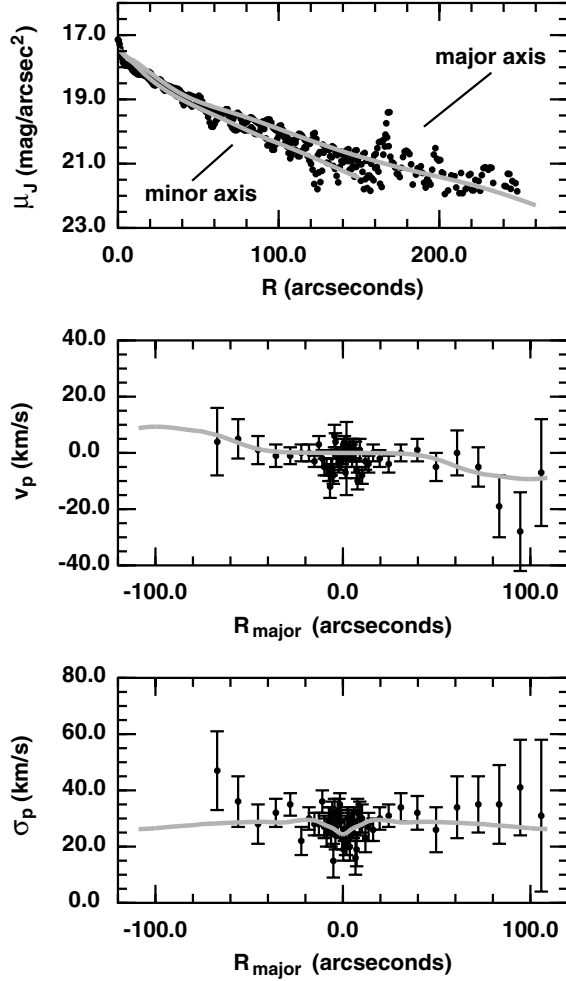


Figure 12. Fit to the streaming velocity along the major axis, v_p , the major- and minor-axis velocity dispersion, σ_p , and the J -band surface brightness, μ_J , of NGC 185 with a 3I dynamical model with inclination $i = 50^\circ$. The black dots are the data points, and the grey curves correspond to the model. The model was fitted to the surface brightness on a grid covering the whole face of the galaxy, but for clarity we only plot the major- and minor-axis profiles in this figure.

10 Gyr as a rough estimate for the mean age of the stellar population (Martínez-Delgado, Aparicio & Gallart 1999), the stellar mass-to-light ratio is $(M/L)_J \sim 1.5 M_\odot/L_{\odot,J}$ or $(M/L)_B \sim 2.1 M_\odot/L_{\odot,B}$ (Worthey 1994). In other words, NGC 185 consists of about 60 per cent luminous matter, by mass, and of 40 per cent dark matter.

3.3.3 The internal dynamics

The stellar density and the radial, tangential and vertical components of the velocity dispersion tensor of the best-fitting models for NGC 185 are presented in Fig. 13. The velocity dispersion tensor of the edge-on model ($i = 90^\circ$; see left-hand column of Fig. 13) has a remarkably large vertical velocity dispersion, peaking up to $\sigma_z \sim 40 \text{ km s}^{-1}$, in the inner parts of the galaxy. This feature is not just an oddity of this one dynamical model but is common to all edge-on models we fitted to NGC 185. Since within the context of axisymmetric models, viewed edge-on, the vertical velocity dispersion is determined almost solely by the photometry, we have to conclude that if NGC 185 is viewed edge-on, it can only maintain its round

shape by having the vertical velocity dispersion much larger than the radial velocity dispersion, which is set by the observed major-axis velocity dispersion. The model with $i = 50^\circ$ and an intrinsic axial ratio $q_{\text{intr}} = 0.62$ is the most nearly isotropic of all models we constructed for NGC 185 (see the middle column of Fig. 13). The rotation velocity of the stars flattens at about 22 km s^{-1} in this model, versus a rotation velocity of 8 km s^{-1} in the edge-on model. Since (i) the intrinsic axial ratio of this model is still fairly close to the peak of the intrinsic shape distribution of dEs, and (ii), like the best-fitting models for NGC 147 and 205, it is very nearly isotropic, this is our preferred best model for NGC 185. The intrinsically very flattened model, with $q_{\text{intr}} = 0.5$ and $i = 45^\circ$ (see the right-hand column of Fig. 12) has a much larger rotation velocity; its peak projected rotation velocity is somewhat higher than that of the $i = 90^\circ$ model but still safely within the error bars. The vertical velocity dispersion σ_z is now much smaller than in the less inclined models. Although this model agrees with the observations to within the (quite substantial) error bars, it fails to reproduce the outward rise of the major-axis velocity dispersion. Hence, with better data it should be possible to better constrain the inclination of NGC 185 on purely dynamical grounds.

4 CONCLUSIONS

In this paper, we present dynamical models for NGC 147, 185 and 205. NGC 205 and 147 have already a flattened apparent shape, so we modelled them assuming them to be viewed edge-on ($i = 90^\circ$). NGC 185, on the other hand, has a much rounder projected shape than the two other Local Group dEs, so we produced models for it assuming inclination angles $i = 90^\circ, 60^\circ, 55^\circ, 50^\circ$ and 45° .

From the range of models that is compatible with the data at the 95 per cent confidence level, we estimate the mass of NGC 205 within a $2R_e$ radius sphere at $M(2R_e) = 10.2^{+3.3}_{-2.0} \times 10^8 M_\odot$, corresponding to a J -band mass-to-light ratio within the inner $2R_e$ of $(M/L)_J = 2.2^{+0.7}_{-0.4} M_\odot/L_{\odot,J}$ or a B -band mass-to-light ratio of $(M/L)_B = 4.5^{+1.5}_{-0.9} M_\odot/L_{\odot,B}$. The best-fitting 3I model for NGC 205 very accurately reproduces the photometric and kinematical data, such as the very bright nucleus and the central drop in the velocity dispersion. Overall, the velocity dispersion tensor is quite isotropic. Only beyond a radius of 0.8 kpc does the tangential anisotropy increase to keep up with the observed rise of the projected velocity dispersion along the major axis. The very bright nucleus shows up in the model as spherically symmetric, dynamically very cold substructure, which can be modelled as an isotropic star cluster with a total mass of $1.36 \times 10^6 M_\odot$, a one-dimensional velocity dispersion $\sigma \approx 7 \text{ km s}^{-1}$ and a truncation radius of about 50 pc. Thus, the nucleus of NGC 205 is structurally and dynamically not unlike a massive globular cluster.

We estimate the total mass of NGC 147 within a $2R_e$ radius sphere at $M(2R_e) = 3.0^{+2.4}_{-1.8} \times 10^8 M_\odot$, corresponding to a J -band mass-to-light ratio within the inner $2R_e$ of $(M/L)_J = 3.4^{+2.7}_{-2.0} M_\odot/L_{\odot,J}$ or a B -band mass-to-light ratio of $(M/L)_B = 4.0^{+3.2}_{-2.4} M_\odot/L_{\odot,B}$. As in the case of NGC 205, the velocity dispersion tensor of the best-fitting model for NGC 147 is remarkably isotropic.

We estimate the total mass of NGC 185 within a $2R_e$ radius sphere at $M(2R_e) = 2.6^{+0.8}_{-0.6} \times 10^8 M_\odot$, corresponding to a J -band mass-to-light ratio within the inner $2R_e$ of $(M/L)_J = 2.2^{+0.6}_{-0.5} M_\odot/L_{\odot,J}$ or a B -band mass-to-light ratio of $(M/L)_B = 3.0^{+1.0}_{-0.7} M_\odot/L_{\odot,B}$. The model with $i = 50^\circ$ has an intrinsic flattening that is still close to the peak of the intrinsic shape distribution of dEs and it, like the best-fitting models for NGC 147 and 205, is nearly isotropic. Therefore, this is our preferred model for NGC 185.

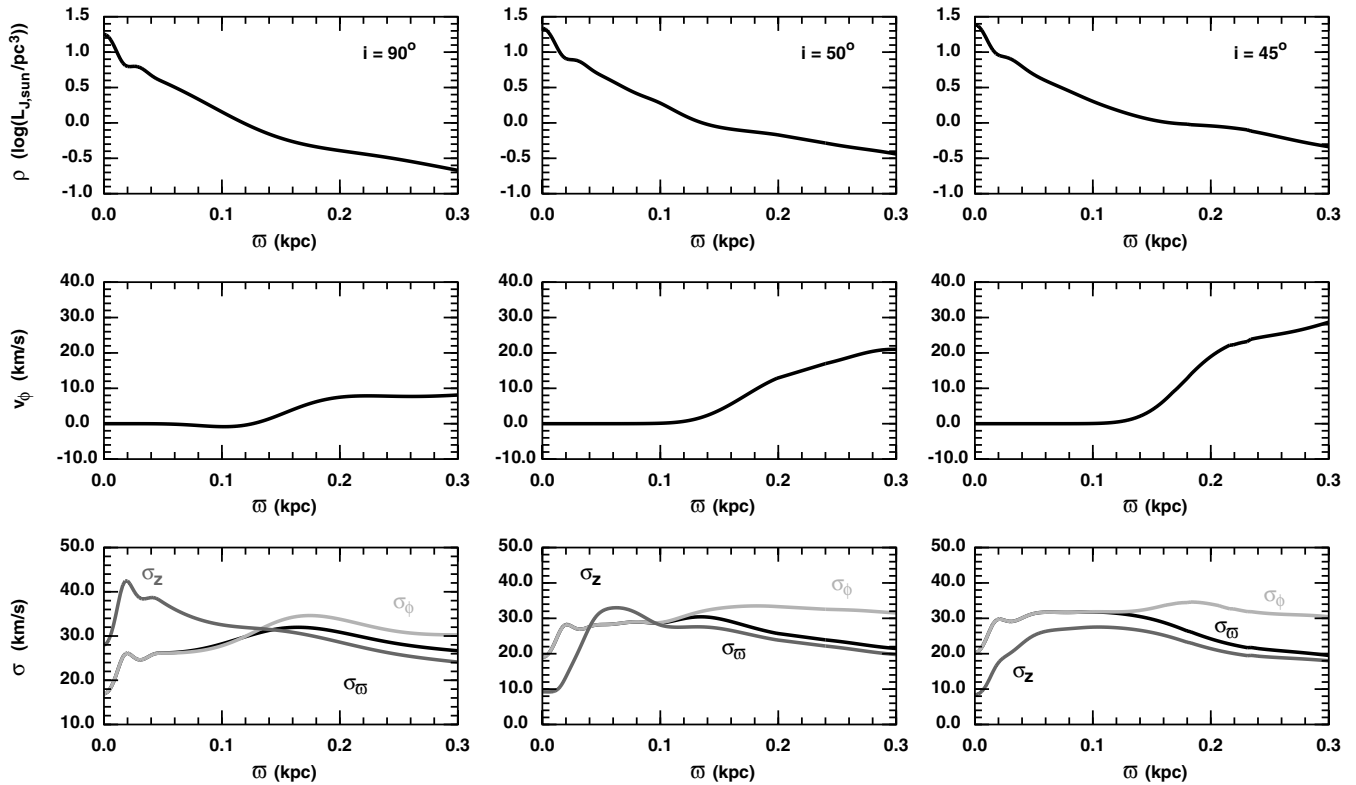


Figure 13. The internal dynamics of the best-fitting models for NGC 185. In the left-hand column, all quantities are plotted for the edge-on model (inclination $i = 90^\circ$); in the middle column, the same dynamical quantities are plotted for the best model with inclination $i = 50^\circ$; in the right-hand column, the best model with inclination $i = 45^\circ$ is presented. Top panels: the logarithm of the luminosity density of the stars, ρ ; middle panels: the rotation velocity, v_ϕ ; bottom panels: the radial, tangential and vertical components of the velocity dispersion tensor. All quantities are plotted as a function of radius within the equatorial plane.

Summarizing our dynamical models for the three Local Group dEs show them to have nearly isotropic velocity dispersion tensors. They have very similar mass-to-light ratios, of the order of $(M/L)_B \sim 4 M_\odot/L_{\odot,B}$. While this is still larger than the expected mass-to-light ratio of the stellar populations of these galaxies, it is about a factor of 2 smaller than the mass-to-light ratios derived by many previous studies. This rather large difference is due in part to differences in the data analysis. Depending on the spectral resolution, the signal-to-noise ratio of the spectra and the method of extracting kinematical data from the spectra, the velocity dispersion estimates for the same galaxy can differ by a factor of 1.5–2 between different authors, with lower resolution observations tending to yield higher values for the velocity dispersion. This, exacerbated by the difficulty of measuring core radii and surface brightnesses of such diffuse objects, required for use in the standard King formula (Richstone & Tremaine 1986), seems to account for at least part of the large spread on the M/L estimates. Therefore, these dwarf galaxies contain much less dark matter than was believed to be the case up to now. Still, within the inner two half-light radii, about 40–50 per cent of the mass is in the form of dark matter, so dEs contain as much dark matter as bright ellipticals. Indeed, Gerhard et al. (2001) produced dynamical models for a sample of 21 luminous ellipticals and found that the dark matter contributes 10–40 per cent of the mass within $1R_e$ and equal interior mass of dark and luminous matter occurs at $2 - 4R_e$.

ACKNOWLEDGMENTS

This research has made use of the NASA/IPAC Infrared Science Archive, which is operated by the Jet Propulsion Laboratory,

California Institute of Technology, under contract with the National Aeronautics and Space Administration. We thank the referee for his constructive remarks.

REFERENCES

- Baade W., 1944a, *ApJ*, 100, 137
- Baade W., 1944b, *ApJ*, 100, 147
- Bender R., Paquet A., Nieto J.-L., 1991, *A&A*, 246, 349
- Binggeli B., Popescu C., 1995, *A&A*, 298, 63
- Butler D. J., Martínez-Delgado D., 2005, *AJ*, 129, 2217
- Carter D., Sadler E. M., 1990, *MNRAS*, 245, 12P
- Choi P. I., Guhathakurta P., Johnston K., 2002, *AJ*, 124, 310
- De Bruyne V., Dejonghe H., Pizzella A., Bernardi M., Zeilinger W. W., 2001, *ApJ*, 546, 903
- Dejonghe H., 1989, *ApJ*, 343, 113
- Dejonghe H., de Zeeuw T., 1988, *ApJ*, 329, 720
- Dejonghe H., Merritt D., 1992, *ApJ*, 391, 531
- Dejonghe H., De Bruyne V., Vauterin P., Zeilinger W. W., 1996, *A&A*, 306, 363
- de Vaucouleurs G., de Vaucouleurs A., Corwin H. G. Jr, Buta R. J., Paturel G., Fouque P., 1991, *Third Reference Catalogue of Bright Galaxies*, Version 3.9
- Evans N. W., Collett J. L., 1994, *ApJ*, 420, L67
- Ferguson H. C., Binggeli B., 1994, *A&ARv*, 6, 67
- Franx M., Illingworth G., Heckman T., 1989, *ApJ*, 344, 613
- Geha M., Guhathakurta P., van der Marel R. P., 2002, *AJ*, 124, 3073
- Geha M., Guhathakurta P., Rich R. M., Cooper M. C., 2006, *AJ*, 131, 332
- Gerhard O., Binney J., 1996, *MNRAS*, 279, 993
- Gerhard O., Kronawitter A., Saglia R. P., Bender R., 2001, *AJ*, 121, 1936

- Han M., Hoessel J. G., Gallagher J. S., III, Holtzman J., Stetson P. B., 1997, AJ, 113, 1001
- Held E. V., Mould J. R., de Zeeuw P. T., 1990, AJ, 100, 415
- Held E. V., de Zeeuw T., Mould J., Picard A., 1992, AJ, 103, 851
- Hodge P. W., 1973, ApJ, 182, 67
- Jarrett T. H., Chester T., Cutri R., Schneider S. E., Huchra J. P., 2003, AJ, 125, 525
- Jones D. H. et al., 1996, ApJ, 466, 742
- Klypin A., Zhao H., Somerville R. S., 2002, ApJ, 573, 597
- Koleva M., Bavouzet N., Chilingarian I., Prugniel P., 2006, in Kissler-Patig M., Walsh J., eds, Scientific Perspectives for 3D Spectroscopy. Springer, Berlin, in press (astro-ph/0602362)
- Lee M. G., 1996, AJ, 112, 1438
- Lee M. G., Freedman W. L., Madore B. F., 1993, AJ, 106, 964
- Lotz J. M., Telford R., Ferguson H. C., Miller B. W., Stiavelli M., Mack J., 2001, ApJ, 552, 572
- Martínez-Delgado D., Aparicio A., 1998, AJ, 115, 1462
- Martínez-Delgado D., Aparicio A., Gallart C., 1999, ApJ, 118, 2229
- McConnachie A. W., Irwin M. J., Ferguson A. M. N., Ibata R. A., Lewis G. F., Tanvir N., 2005, MNRAS, 356, 979
- Merritt D., Quinlan G. D., 1998, ApJ, 498, 625
- Messier C., 1798, Observations Astronomiques, 1770–1774, Connaissance des Temps pour l'an IX, 461
- Mould J. R., Kristian J., Da Costa G. S., 1983, ApJ, 270, 471
- Peletier R. F., 1993, A&A, 271, 51
- Prugniel P., Soubiran C., 2001, A&A, 369, 1048
- Read J. I., Wilkinson M. I., Evans N. W., Gilmore G., Kleyna J. T., 2006, MNRAS, 366, 429
- Renzini A., 1993, AJ, 115, 2459
- Richer M. G., McCall M. L., Stasińska G., 1998, A&A, 340, 67
- Richstone D. O., Tremaine S., 1986, AJ, 92, 72
- Simien F., Prugniel Ph., 2002, A&A, 384, 371
- Tremaine S. D., Ostriker J. P., Spitzer L., 1975, ApJ, 196, 407
- Valluri M., Ferrarese L., Merritt D., Joseph C. L., 2005, ApJ, 628, 137
- van den Bergh S., 1998, AJ, 116, 1688
- Worthey G., 1994, ApJS, 95, 107

APPENDIX A: THE THREE-INTEGRAL COMPONENTS

For a given potential, we wish to find the DF that best reproduces the kinematical information. As a first step, the DF is written as a weighted sum of basis functions, called ‘components’. Here, we use components of the form

$$F^{i,\epsilon_i}(E, I_2, I_3) = (E - E_{0,i})^{\sigma_i} (I_2 - I_{0,i})^{\tau_i} I_3^{\rho_i},$$

$$\text{if } E > E_{0,i}, \epsilon_i I_2 > I_{0,i} \geq 0$$

$$= 0, \quad \text{if } E \leq E_{0,i} \text{ or } \epsilon_i I_2 \leq I_{0,i} \quad (\text{A1})$$

with σ_i , τ_i , and ρ_i integer numbers. $E_{0,i}$ is a lower bound on the binding energy, which defines the outer boundary within which the component is non-zero. The condition $\epsilon_i I_2 > I_{0,i} \geq 0$, with $\epsilon_i \in [-1, +1]$ defines the ‘handedness’ of the component. If $\epsilon_i = +1$, only orbits with positive angular momentum $I_2 > I_0$ are populated and we call the component $F^{i,+}$ ‘right-handed’. If $\epsilon_i = -1$, only orbits with negative angular momentum $I_2 < -I_0$ are populated and the component $F^{i,-}$ is ‘left handed’. Components that populate prograde and retrograde orbits equally, labelled with $\epsilon_i = 0$, are constructed as $F^{i,0}(E, I_2, I_3) = F^{i,+}(E, I_2, I_3) + F^{i,-}(E, I_2, I_3)$. Components with $I_0 \neq 0$ and $E_0 \neq 0$ populate orbits within a torus-shaped region of space.

The spatial velocity moments, $\mu_{2l,m,2n}^{i,+}(\varpi, z)$, of the component $F^{i,+}(E, I_2, I_3)$ are given by

$$\mu_{2l,m,2n}^{i,+}(\varpi, z) = \int F^{i,+}(E, I_2, I_3) v_\lambda^{2l} v_\phi^m v_z^{2n} dv_\lambda v_\phi v_z \quad (\text{A2})$$

$$= \frac{2^{l+n+(m+1)/2}}{\varpi^{m+1}(\lambda - v)^{l+n}} \int_{E_{0,i}}^\psi (E - E_{0,i})^{\sigma_i} dE$$

$$\times \int_{I_{0,i}}^{\varpi^2(\psi - E)} I_2^{(m-1)/2} (I_2 - I_{0,i})^{\tau_i} dI_2$$

$$\times \int_{I_3^-}^{I_3^+} I_3^{\rho_i} (I_3^+ - I_3)^{l-1/2} (I_3 - I_3^-)^{n-1/2} dI_3, \quad (\text{A3})$$

with

$$I_3^+ = (\lambda + \gamma) \left[G(\lambda) - E - \frac{I_2}{\lambda + \alpha} \right], \quad (\text{A4})$$

$$I_3^- = (v + \gamma) \left[G(v) - E - \frac{I_2}{v + \alpha} \right]. \quad (\text{A5})$$

This integration can be performed analytically by repeatedly using the lemma

$$\int_a^b x^i (b-x)^j (x-a)^k dx = B(k+1, j+1)$$

$$\times (b-a)^{j+k+1} b^j {}_2F_1 \left(-i, j+1; j+k+2; 1 - \frac{b}{a} \right), \quad (\text{A6})$$

with B the Euler beta function and ${}_2F_1$ the hypergeometric function. Thus, one obtains the following expression for the spatial velocity moments:

$$\mu_{2l,m,2n}^{i,+}(\varpi, z)$$

$$= \mathcal{F}_{l,m,n}^i \varpi^{2\tau_i} \left(\psi - E_{0,i} - \frac{I_{0,i}}{\varpi^2} \right)^{\sigma_i + \tau_i + n + l + 2}$$

$$\times (\psi - E_{0,i})^{(m-1)/2} [(\lambda + \gamma)(G(\lambda) - E_{0,i})]_i^{\rho_i}$$

$$\times \sum_{r=0}^{\rho_i} \frac{(-\rho_i)_r (l+1/2)_r}{r! (\sigma_i + \tau_i + n + l + 3)_r}$$

$$\left[\frac{(\lambda - v)(\psi - E_{0,i} - I_{0,i}/\varpi^2)}{(\lambda + \gamma)(G(\lambda) - E_{0,i})} \right]^r$$

$$\times \sum_{s=0}^{\rho_i - r} \frac{(r - \rho_i)_s (\sigma_i + 1)_s}{s! (\sigma_i + \tau_i + n + l + r + 3)_s} \left[\frac{\psi - E_{0,i} - I_{0,i}/\varpi^2}{G(\lambda) - E_{0,i}} \right]^s$$

$$\times \sum_{p=0}^{\rho_i - r - s} \frac{(r + s - \rho_i)_p}{p!} \left[\frac{(\alpha + v)(\psi - E_{0,i})}{(\alpha - \gamma)(G(\lambda) - E_{0,i})} \right]^p$$

$$\times {}_2F_1 \left(-p - \frac{m-1}{2}, \sigma_i + \tau_i + n + l + r + s + 2; \right.$$

$$\left. \sigma_i + \tau_i + n + l + r + s + 3; 1 - \frac{I_{0,i}}{\varpi^2(\psi - E_{0,i})} \right) \quad (\text{A7})$$

with the forefactor $\mathcal{F}_{l,m,n}^i$ given by

$$\mathcal{F}_{l,m,n}^i =$$

$$2^{n+l+(m+1)/2} \frac{\Gamma(\sigma_i + 1) \Gamma(\tau_i + 1) \Gamma(n + \frac{1}{2}) \Gamma(l + \frac{1}{2})}{\Gamma(\sigma_i + \tau_i + n + l + 3)}. \quad (\text{A8})$$

The velocity moments of the left-handed component $F^{i,-}(E, I_2, I_3)$, $\mu_{2l,m,2n}^{i,-}$, are linked to those of its right-handed analogue $F^{i,+}(E, I_2, I_3)$ via the relation $\mu_{2l,m,2n}^{i,-} = (-1)^m \mu_{2l,m,2n}^{i,+}$. The spatial velocity moments with respect to the cylindrical velocity components v_ϖ , v_ϕ and v_z can be constructed from the moments $\mu_{2l,m,2n}^{i,\epsilon_i}$ using the transformation

$$\begin{bmatrix} v_\varpi \\ \text{sign}(z) v_z \end{bmatrix} = \begin{pmatrix} \cos \Theta & -\sin \Theta \\ \sin \Theta & \cos \Theta \end{pmatrix} \begin{pmatrix} v_\lambda \\ v_\nu \end{pmatrix} \quad (\text{A9})$$

with

$$\cos \Theta = \sqrt{\frac{(v + \alpha)(\lambda + \gamma)}{(\alpha - \gamma)(\lambda - v)}}, \quad \sin \Theta = \sqrt{\frac{(\lambda + \alpha)(v + \gamma)}{(\gamma - \alpha)(\lambda - v)}}. \quad (\text{A10})$$

This paper has been typeset from a $\text{\TeX}/\text{\LaTeX}$ file prepared by the author.